

## ARTICLE OPEN

Zoology of domain walls in quasi-2D correlated charge density wave of 1T-TaS<sub>2</sub>Jae Whan Park<sup>1</sup>✉, Jinwon Lee<sup>1,2</sup> and Han Woong Yeom<sup>1,2</sup>✉

Domain walls in correlated charge density wave compounds such as 1T-TaS<sub>2</sub> can have distinct localized states which govern physical properties and functionalities of emerging quantum phases. However, detailed atomic and electronic structures of domain walls have largely been elusive. We identify using scanning tunneling microscope and density functional theory calculations the atomic and electronic structures for a plethora of discommensuration domain walls in 1T-TaS<sub>2</sub> quenched metastably with nanoscale domain wall networks. The domain walls exhibit various in-gap states within the Mott gap but metallic states appear in only particular types of domain walls. A systematic understanding of the domain-wall electronic property requests not only the electron counting but also including various intertwined interactions such as structural relaxation, electron correlation, and charge transfer. This work guides the domain wall engineering of the functionality in correlated van der Waals materials.

npj Quantum Materials (2021)6:32; <https://doi.org/10.1038/s41535-021-00330-9>

## INTRODUCTION

Metal-insulator transitions and the emergence of superconductivity and other exotic quantum phases from strongly interacting electronic systems are central issues in condensed matter physics and important for device applications. Such interacting electronic systems are recently attracting particular interest in two-dimensional (2D) materials with the extraordinary tunability provided<sup>1–3</sup>. In particular, quasi 2D charge-density-wave (CDW) compounds and their monolayer versions with strong interactions are under the focus of huge research activity because of rich quantum phases emerging from the commensurate CDW (CCDW) ground state with exotic electronic properties such as a spin frustrated Mott insulator in 1T-TaS<sub>2</sub> and an excitonic insulator in 1T-TiSe<sub>2</sub><sup>4,5</sup>. Suppressing the CCDW order in these materials by heat, pressure, doping, ultrafast optical, and electrical pulses leads to various quasi-metallic metastable phases which consist of CCDW domains and discommensuration domain walls (DWs)<sup>6–28</sup>. The electronic properties of these ‘frustrated’ phases have been known to be governed by electronic states residing on DWs created<sup>24–28</sup>. Those topological in-gap states have been suggested to play crucial roles in the emerging superconductivity<sup>26–29</sup> and the memristic resistivity switching of DW phases<sup>14</sup>.

In this work, we focus on the DW phases excited from the Mott CDW ground state of 1T-TaS<sub>2</sub><sup>30–32</sup> with strong electron correlation<sup>4</sup> and strong spin frustration<sup>33,34</sup>. The atomic structure of CCDW in 1T-TaS<sub>2</sub> has a unit of the David-star (DS) cluster with a  $\sqrt{13} \times \sqrt{13}$  supercell<sup>35</sup>, which features one unpaired electron in the central Ta atom. This electron has been known to fall into a spin-frustrated Mott-insulator state by the onsite Coulomb repulsion<sup>4</sup>. A recent STS study observed two types of isolated DWs among the various types of DW configuration<sup>18,19</sup>, as line defects within this ‘correlated’ CCDW phase, which have insulating electronic states due to strong electron correlation and structural relaxation within them<sup>36</sup>. Above 180 K, the Mott insulating CCDW phase transits spontaneously into a metallic phase with a nanoscale honeycomb DW network, which is called a nearly-commensurate CDW (NCCDW) phase<sup>29,37–42</sup>. Our recent work

identified this DW with another type of structure and a metallic in-gap state<sup>29</sup>, which is absolutely different from the two types of insulating DWs within the CCDW phase<sup>36</sup>. A theoretical model was suggested<sup>29,43</sup> to connect it to the emerging superconductivity from this phase under pressure and doping<sup>26</sup>. This series of recent research revealed the various electronic properties and huge structural degrees of freedom within DWs of 1T-TaS<sub>2</sub> CDW phases. However, only a small fraction of DWs are identified among those expected from the large (at least thirteen-fold) degeneracy of the CDW structure and a systematic understanding of their diversity and complexity has been lacking. This information would be essential for the controllability over the functionality and the emerging or hidden phases brought by DWs<sup>10–13</sup>.

In this paper, we explore the structural and electronic properties of the 1T-TaS<sub>2</sub> surface layer, which was manipulated by scanning tunneling microscope (STM) voltage pulses into nanoscale metastable DW networks. The metastable DW networks are endowed with an enhanced variety of DWs<sup>18,19</sup>. We identify more than ten different DW structures and their topological vertices. The atomic structures and electronic states of most of these DWs are determined by direct comparisons of STM data and density functional theory (DFT) calculations. A systematic understanding of the structural and electronic variety of DWs is obtained through extensive DFT calculations, which unravel the diverse interactions involved such as structural relaxations, electron correlation effect, and charge transfer from neighboring domains.

## RESULTS

## Domain walls and their network in the nanoscale quenched phase

Various types of DWs are found in the quenched phase of Fig. 1a, b, which are created by applying a positive voltage pulse from an STM tip<sup>32</sup>. It consists of domains of a few tens of nanometers in the CCDW structure as separated by various different DWs. These DWs form an irregular network extending laterally to a size of up to a few hundred nanometers depending on the pulse voltage.

<sup>1</sup>Center for Artificial Low Dimensional Electronic Systems, Institute for Basic Science (IBS), Pohang, Republic of Korea. <sup>2</sup>Department of Physics, Pohang University of Science and Technology (POSTECH), Pohang, Republic of Korea. ✉email: [absolute81@ibs.re.kr](mailto:absolute81@ibs.re.kr); [yeom@postech.ac.kr](mailto:yeom@postech.ac.kr)

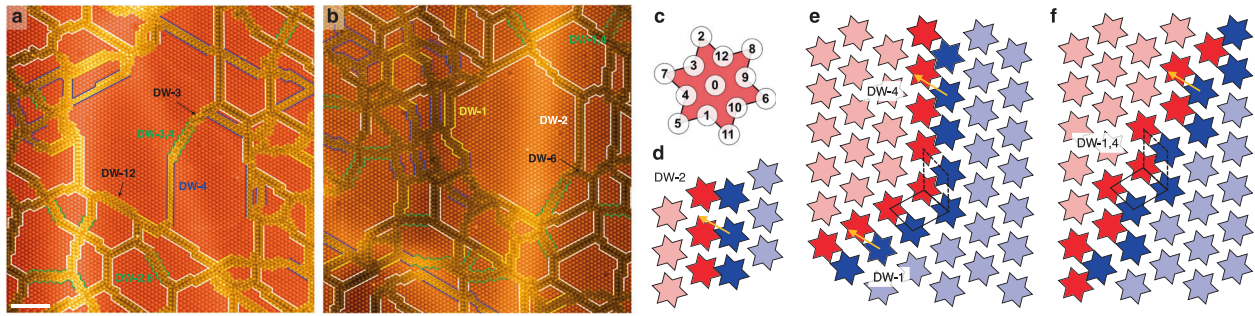


**Fig. 1** Domain and domain-wall structures in quenched 1T-TaS<sub>2</sub>. **a** and **b** Two independent STM images (sample bias voltage  $V_s = -1.2$  V, tunneling current  $I_t = 10$  pA, size  $L^2 = 80 \times 80$  nm<sup>2</sup>, scale bar = 10 nm). The line colors denote the type of domain wall: DW-1: yellow, DW-2: white, DW-4: blue, and zigzag domain wall: green. **c** David-star cluster of the CCDW phase with thirteen Ta atoms indexed. A DW is defined as the center of DS clusters of the neighboring domain sits on Ta atomic sites of 1–12, which is indexed as DW-1–DW-12, respectively. **d–f** Schematic arrangement of David stars for the domain walls. **d** DW-2, **e** DW-1, and **f** zigzag domain wall (DW-1,4). Orange arrows denote the CCDW vector. Solid (dashed) parallelogram in **e** denotes the domain-wall unit of DW-1 (DW-4).

**Table 1.** Energetics and electronic structure of all twelve *straight* domain walls.

|                            | DW-7   | DW-5   | DW-4A (DW-4B)   | DW-3   | DW-2   | DW-1   | DW-12  | DW-11  | DW-10  | DW-9   | DW-8   | DW-6   |
|----------------------------|--------|--------|-----------------|--------|--------|--------|--------|--------|--------|--------|--------|--------|
| Number of Ta               | −7     | −5     | −4              | −3     | −2     | −1     | 1      | 2      | 3      | 4      | 5      | 7      |
| $E_{\text{PBE}+U}$ (eV/DS) | 0.107  | 0.085  | 0.033 (0.044)   | 0.058  | 0.025  | 0.039  | 0.069  | 0.059  | 0.042  | 0.058  | 0.047  | 0.048  |
| $E_{\text{PBE}}$ (eV/DS)   | 0.079  | 0.069  | 0.022 (0.027)   | 0.040  | 0.010  | 0.023  | 0.061  | 0.045  | 0.052  | 0.063  | 0.038  | 0.068  |
| LHS                        | −0.080 | −0.057 | −0.042 (−0.054) | −0.126 | −0.121 | −0.041 | −0.107 | −0.226 | −0.087 | −0.172 | −0.098 | −0.084 |
| UHS                        | 0.301  | 0.302  | 0.320 (0.322)   | 0.270  | 0.251  | 0.327  | 0.270  | 0.144  | 0.309  | 0.219  | 0.274  | 0.290  |
| Character                  | M      | M      | I (M)           | I      | I      | M      | M      | M      | I      | I      | I      | I      |

Formation energy is defined by  $E = E_{\text{DW}}/N - E_{\text{CCDW}}$ , where  $E_{\text{DW}}$  and  $E_{\text{CCDW}}$  are the total energies and  $N$  is the number of the David-star clusters in the supercell.  $E_{\text{PBE}}$  and  $E_{\text{PBE}+U}$  are obtained from the exclusion and inclusion of the extra electron correlation  $U$ , respectively. LHS and UHS are the lower and upper Hubbard states at the domain region of the supercell, respectively. For the CCDW phase, the LHS (UHS) locates at  $-0.216$  ( $+0.198$ ) eV. M and I stand for metal and insulators.

Most DWs are formed straightly along the CCDW unit vector with a single-phase shift between two adjacent CCDW domains. Due to the thirteen Ta atoms in the DS cluster, there are twelve possible *straight* DW configurations and the notation of DWs are defined as the relative position of the center DS clusters between two adjacent domains as shown in Fig. 1c and Supplementary Fig. 1. We also found the *zigzag* type of DWs, which can be defined by two alternating phase-shift vectors, one of which is rotated by 60° with respect to the other (see Fig. 1f). Thus, the *zigzag* DWs are rotated by 30° with respect to the *straight* DW. The twelve possible *zigzag* DW configurations are summarized in Supplementary Fig. 1. The DWs also construct the complex DW junctions including the X, Y, and + shape (Supplementary Fig. 2). The honeycomb-like network of DWs can be seen as the combination of Y-shaped junctions (Supplementary Fig. 3). The detailed properties of DWs will be discussed further below.

### Population and energetics of domain walls

Among the twelve possible *straight* DW configurations, we found six types of DWs in the quenched phase. The second-type DW (DW-2) is the most popular DW structure and DW-4 and DW-1 are also frequently found. These DWs were already observed in the CCDW phase at low temperature (DW-2 and DW-4) and in the NCCDW phase at room temperature (DW-1)<sup>18,29,36</sup>. Three minor DWs of DW-3, DW-6, and DW-12 appear sparsely with shorter lengths, but the other six possible *straight* DWs cannot be found in the present STM images. Interestingly, the *zigzag* type of DWs is rather popular (less than DW-4 but more than DW-1) with relatively long DW lengths. We found three types of *zigzag* DWs, namely, DW-2,8, DW-1,4, and DW-3,4. The two indices given here indicate the two-phase shift vectors defining a *zigzag* DW (Fig. 1f).

We optimize the atomic structures of all twelve configurations of *straight* DWs by DFT calculations. The resulting energetics and electronic properties are summarized in Table 1. The fully relaxed DFT calculations predict that DW-2 is the most stable structure and the second-lowest energy configurations of DW-1 and DW-4 almost degenerate in energy. This energetic hierarchy is largely consistent with the observed population of major DWs. However, the present calculations cannot explain all the population details of the minor DWs of the DW-3, DW-6, and DW-12 and the other absent DWs in the experiment. This may be due to their short lengths and various boundary conditions imposed by neighboring domains, DWs, and DW junctions. In addition, we also observe that the energetically unfavored DWs, such as DW-5, DW-8, and DW-6 break into two DWs of lower energies as shown in Fig. 2. This partly explains the absence of the unfavored DWs. The energy costs of *zigzag* DWs (0.025, 0.028, and 0.030 eV/DS for DW-2,8, DW-1,4, and DW-3,4, respectively) are comparable to those of major *straight* DWs. This seems roughly consistent with their popularity in the experiment, being popular than the minor *straight* DWs. The present results indicate the importance of detailed atomic structures in understanding the DW phases.

### Atomic structures of straight domain walls

The atomic structure of DW-2 in Fig. 3b is composed of two imperfect DS clusters of a similar shape, each with 12 Ta atoms but with distinct numbers, five (left) and six (right), of S atoms. Since bright protrusions in STM images represent top-layer S atoms, the different numbers of S atoms are well reflected in the corresponding STM images; larger triangular clusters and smaller imperfect triangles in the left and the right side of the DW, respectively (Fig. 3f). These STM images are well reproduced in the

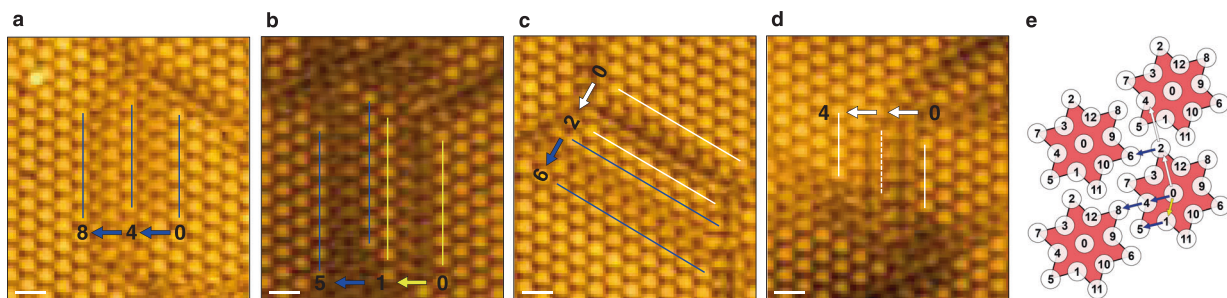


**Fig. 2** **Narrow domains between stable domain walls.** **a** A single-row domain with two DW-4 structures instead of DW-8 (scale bar = 2 nm). **b** A double-row domain with DW-1 and DW-4 structures instead of DW-5. **c** A double-row domain with DW-2 and DW-4 structures instead of DW-6. **d** Direct connected two DW-2 structures without a domain. **e** Corresponding phase shift vectors on the David-star clusters.

simulated STM images, especially the asymmetric double rows along with the DW. The present double row structure is distinguishable from the previously suggested model with a single row<sup>36</sup>. These two models are very close in their energies, with only 9 meV difference per supercell, and their electronic structures are very similar. Thus, these structures may coexist (Supplementary Fig. 4), while we find the double row model to reproduce better the STM images observed.

The STM image of DW-4 exhibits also an asymmetric double row (named as DW-4B) of imperfect DS clusters with 22 Ta atoms (the lower part of Fig. 3g). Very interestingly, we find that this double row structure changes abruptly to a single row structure (DW-4A) with the same phase shift between neighboring domains (Fig. 3g). This evidences that a DW can have a few competing structures, due to its own internal structural degree of freedom. Our DFT calculation tells that the single-row structure (DW-4A) is formed with a single imperfect DS cluster (with nine Ta atoms) and distorted DS clusters at the neighboring domain edge. This structure is consistent with the previous structural model<sup>36</sup>, and it is more stable (~56 meV/supercell) than the double row (DW-4B) structure. The optimized atomic structures of DW-4A and DW-4B reproduce the observed STM images well. We also find another type of a single-row DW structure without a strong distortion of the domain edge, which is slightly less stable (~29 meV/supercell) than the above DW-4A structure. However, its electronic structure is not consistent with previous STS spectra<sup>36</sup> (Supplementary Fig. 9).

The DW-1 structure comprising 25 Ta atoms is similar to the DW-2 but features an additional Ta atom between two imperfect DS clusters. The corresponding STM image shows rows of three clusters within DW-1 in contrast to the double rows of DW-2 (Fig. 3e). This structure is consistent with our previous work<sup>29</sup>. Other minor DWs also have their characteristic atomic structure, which is determined by their own CDW phase shift vectors and the internal structural relaxation (Supplementary Figs. 5 and 6).

### Electronic structures of straight domain walls

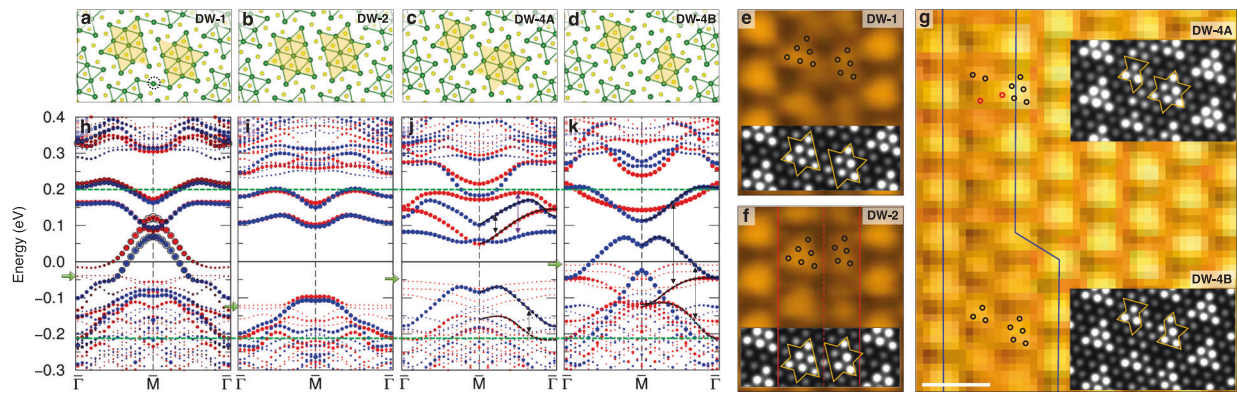
The rich variations in DW structures result in a variety of localized electronic states. All twelve straight DWs exhibit in-gap states localized one-dimensionally along the DWs (Supplementary Fig. 7). The Mott gap of the CCDW phase is, thus, substantially reduced or closed at DWs. However, details of in-gap states depend on various different parameters such as the number of Ta atoms ( $d_z$  electrons) in the DW region, the structural relaxation, the correlation effect, and the charge transfer from neighboring domains. For example, the DW-2 structure exhibits a rather large bandgap (Fig. 3i), which is consistent with the previous STS study<sup>36</sup>. There exist two in-gap states localized along with this DW at about 0.1 and 0.2 eV above the Fermi energy. The majority and minority spin bands for these in-gap states (Fig. 3i) almost degenerate and their band dispersions do not change substantially with the inclusion of the Coulomb energy  $U$  (Supplementary

Fig. 7). That is, the two in-gap states are split trivially by the bonding-antibonding interaction due to the structural relaxation. The insulating property of DW-2 is basically due to the even number of electrons from the two identical imperfect DS unit cells within the DW.

In stark contrast, DW-1 with a similar atomic structure exhibits a metallic behavior with two in-gap bands crossing the Fermi level. These bands are due to an unpaired electron on the additional link Ta atom (marked by the black circle in Fig. 3a), which makes the total electron number within DW-1 odd. As shown in Fig. 3h, the band splitting is due to the local spin and the electron correlation. Except for this Ta atom with partially filled spin-polarized states, the atomic configuration with two identical imperfect DSs, each with twelve Ta atoms, in the DW-1 structure is similar to the DW-2 structure and the band dispersions of corresponding in-gap states above the Fermi level are comparable to each other. This comparison manifests the crucial importance of the number of electrons within a DW unit cell.

The atomic and electronic property of a DW can substantially be affected by the charge transfer in addition to the electron correlation. The single-row structure of DW-4A is endowed with an odd number of Ta atoms and the partially filled orbital is expected on the imperfect DS cluster within the DW. The DW-4A, however, exhibits an insulating character with a bandgap of 0.1 eV due to the charge transfer from the edge of the neighboring domain to the DW: We find that the fully filled state between  $-0.2$  to  $-0.1$  eV (the blue band) is spin-split and localized on one edge atom of the broken DS cluster of the DW (Supplementary Fig. 8). On the other hand, the lower and upper Hubbard states of the domain-edge DS cluster are shifted upward just above the Fermi level (indicated by the purple arrow in Fig. 3j), which is consistent with the previous STS spectra<sup>36</sup>. These behaviors indicate that electrons are transferred from the edge of the neighboring domains to the DW clusters. We further notice that the amount of charge transfer depends on the structural distortion of the DS clusters on domain edges (Supplementary Fig. 9). In the double row structure (DW-4B) of the same domain wall, the DW width becomes large with two broken DS clusters. A band localized at those imperfect clusters becomes partially filled due to the charge transfer from the domain region (indicated by the green arrow in Fig. 3k). The other states on the imperfect DS clusters within the DW open a relatively large bandgap of 0.25 eV with spin-split bands (Supplementary Fig. 8), therefore there is a possibility of the 1D magnetism along with this DW (Supplementary Fig. 10). However, this is closely related to the controversial issue of the magnetic ordering for the CCDW phase<sup>4,33,34,44,45</sup> thus the magnetic ordering predicted in the present calculations for the DWs has to be investigated further by experiments and more sophisticated calculations. The above comparison of two different DW structures for one DW type indicates the importance of the charge transfer between DWs and neighboring domains, as well as the structural degree of freedom. In most of DWs except the DW-11, the Hubbard bands of





**Fig. 3 Atomic and electronic structures of major domain walls.** **a–d** Atomic structure: **a** DW-1, **b** DW-2, **c** DW-4A, and **d** DW-4B. The imperfect DS clusters are marked by the yellow shadows. **e–g** Experimental STM image (scale bar = 2 nm). The circles denote the top S atomic position in the atomic structure. Insets are the theoretical STM simulations. Simulated STM images are obtained by integrating charge density from  $-1.2$  to  $0$  eV (Fermi level) of each optimized structure. The images represent the charge density at a constant height of  $2 \text{ \AA}$  away from the top S atom. Red lines in **f** denote the asymmetric double rows. Blue lines in **g** denote the domain edge of a single (DW-4A) and double rows (DW-4B) domain walls. **h–k** Band structures. Red (Blue) circles denote the spin-majority (minority) states. The circle size is proportional to the localized states at the domain-wall region (shadow DS clusters). Black open circles in **h** are localized states at the linked atom marked by the dashed circle in **a**. Green arrows indicate the lower Hubbard states at domain region. Green dashed lines indicate the upper and lower Hubbard states of the CCD phase for comparison. Purple arrows in **k** indicate the upper and lower Hubbard states of the domain edge. Black solid and dashed arrows in **j** and **k** are guides for the eyes for the spin-polarized bands.

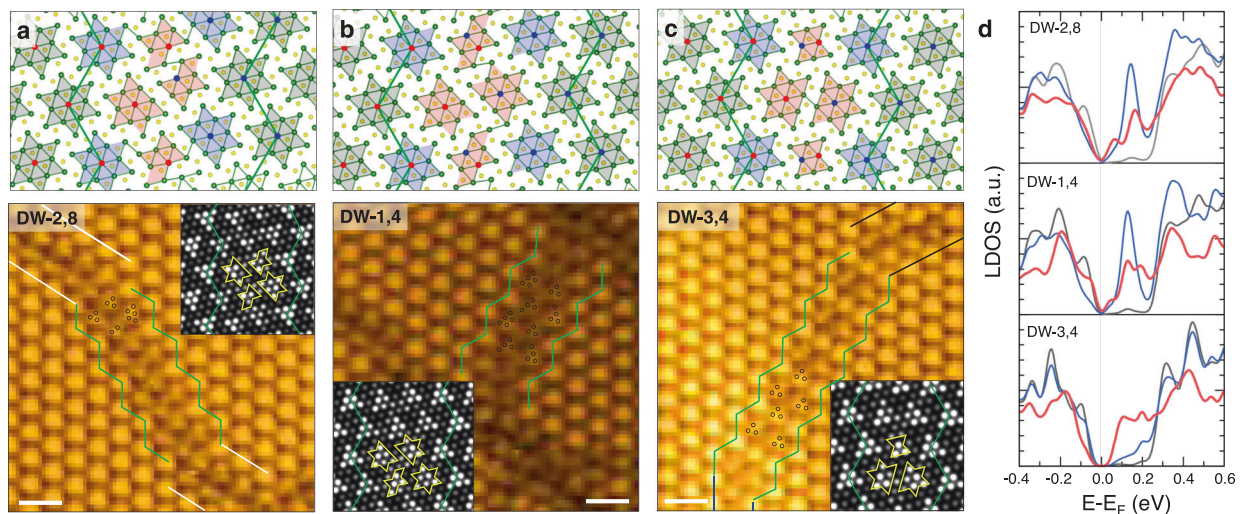


**Fig. 4 Atomic and electronic structure of zigzag domain walls.** **a** DW-2,8, **b** DW-1,4, and **c** DW-3,4. Red and blue dots in atomic structures denote the center site of the David-star cluster of left and right domains, respectively. The bottom panels are experimental STM images (scale bar = 2 nm). Insets are simulated STM images as same as Fig. 3. Green zigzag lines denote the domain edge. **d** Local DOS of DW-2,8, DW-1,4, and DW-3,4. Line colors in **d** correspond to the localized states at the clusters with the same color in atomic structures.

neighboring domains are shifted to higher energy indicating the donation of electrons from domains to DW (Table 1 and Supplementary Fig. 7). This is consistent with the peak shift of Hubbard states at domain edges observed in the previous experiment<sup>36</sup>.

### Zigzag domain walls

Figure 4 shows the atomic structures and STM images of zigzag DWs (DW-2,8, DW-1,4, and DW-3,4). The DW-2,8 and DW-1,4 consist of four types of Ta clusters and the clusters are connected to each other through distortions of outer Ta atoms. The DW-3,4 consists of three types of Ta clusters so that the width is narrower. These STM topographies, which are well reproduced in our DFT simulations, reveal that the zigzag DWs have an even larger structural degree of freedom. There exist two types of in-gap states related to these zigzag DWs, which are localized at DWs (the red lines in Fig. 4d obtained on the broken DW clusters mentioned

above, which is indicated by red clusters in Fig. 4a, b, and c) and edges of neighboring domains (blue lines of Fig. 4d and blue clusters in Fig. 4a, b, and c), respectively. These states cover most of the Mott gap but the local density of states (LDOS) of the whole systems commonly touch zero at the Fermi level, which is close to a pseudogap. Note that the zigzag DWs have the  $\times 2$ -ordered Ta clusters along the DW direction. We attribute the common insulating nature of zigzag DWs to the alternating hopping amplitudes similar to the insulating 1D zigzag dimer chain of the Su-Schrieffer-Heeger model<sup>46</sup>, while we do not establish a quantitative model. The notable difference between DW-3,4 and DW-1,4/DW-2,8 is that the domain edge states of DW-3,4 preserve the Mott insulating character with upper and lower Hubbard states largely while those on DW-2,8 and DW-1,4 show large in-gap states at around  $0.1 \text{ eV}$  without strong spin polarization (Supplementary Fig. 11). This is related to how the DS clusters on

domain edges are distorted due to the neighboring imperfect DS clusters within DWs.

## DISCUSSION

This work provides a totally different approach and understanding from a recent theoretical work, which explained the insulating properties of *straight* DWs of 1T-TaS<sub>2</sub> in terms of the frustrated hopping within the triangular Mott insulator model<sup>47</sup>. In fact, the particular type of DWs mentioned in the previous model is metallic in our experiment and calculation. This discrepancy indicates clearly the limitation of this simple model, which ignores all the internal degrees of freedom of DWs.

This work uses the large tunneling current and bias to induce DW networks. While the mechanism is not fully clear yet, the network may be induced by the local heating or the electric field. The DW phases were also induced globally by different methods of heating<sup>29</sup> and optical pulses<sup>10</sup>. Since each method may have different levels of excitation and thermodynamics, the lateral and population distribution of different types of DWs induced can be different. For example, a recent STM study showed that the optical pulse produces irregular networks of the *zigzag* DWs and DW-2 configurations<sup>48</sup>. This is partly consistent with our work. On the other hand, as we reported recently, the thermally excited DW phase (the NCCDW phase above 180 K) has only the DW-1 type uniformly<sup>29</sup>. Nevertheless, what is very important here is that we tabulate most of the DW structures possible and provide a unified understanding of their properties.

We investigate systematically structural and electronic properties of DW structures of the 1T-TaS<sub>2</sub> surface layer, which was manipulated by scanning tunneling microscope (STM) voltage pulses to generate DW networks with a plethora of metastable DWs<sup>18,19</sup>. We identify more than ten different DW structures including the straight DWs discussed partly in the previous works, the newly observed *zigzag* DWs, and the breakdown of unstable DWs into multiple DWs of lower energy. The atomic structures and electronic states of most of these DWs are determined by direct comparisons of STM data and density functional theory (DFT) calculations including the on-site Coulomb interaction. Various types of DW configurations lead to rich electronic states in a narrow energy scale within the bandgap of 1T-TaS<sub>2</sub>. A systematic understanding of the structural and electronic variety of these DWs is obtained through extensive DFT calculations. The electronic property of these discommensurate DWs exhibits both metallic and insulating characters depending on their atomic structure, correlation, and charge transfer from neighboring domains. Our finding of the DW properties would help to understand the microscopic origins of various metastable phases, hidden phases, and emerging superconductivity, which are all attributed to the electronic states localized on DWs.

## METHODS

### Sample preparations

The single crystal 1T-TaS<sub>2</sub> was grown by iodine vapor transport method in the evacuated quartz tube. Before the growth of the sample, the powder 1T-TaS<sub>2</sub> was sintered for 48 h at 750 °C. We repeated this process two times to get polycrystals. To get a high-quality sample, the seeds were slowly transported by iodine at 900–970 °C for 2 weeks. The tube was rapidly cooled down to room temperature in the air due to the metastability of the 1T phase.

### Experiments

The STM measurements were carried out at  $T = 4.3$  K with a commercial STM (SPECS) and the mechanically sharpened Pt-Ir wires were used for STM tips. All STM images were obtained with the constant current mode and the bias voltage  $V_s$  was applied to the sample. The detailed method of the

textured CDW domain formation and the preparation of single-crystal 1T-TaS<sub>2</sub> are similar to the previous study<sup>18</sup>.

## DFT calculations

The DFT calculations were carried out by using the Vienna ab initio simulation package<sup>49</sup> within the Perdew-Burke-Ernzerhof functional of the generalized gradient approximation<sup>50</sup> and the projector augmented wave method<sup>51</sup>. We used the single-layer model of 1T-TaS<sub>2</sub> with a vacuum spacing of about 13.6 Å. We assumed the 2D-like Mott states at the surface limit based on most of DWs are not coupled between the first and the second layer (Supplementary Fig. 12) and the interlayer coupling of the DWs in a bilayer structure is not affecting substantially the electronic structure of the DWs (Supplementary Fig. 13). A plane-wave basis set of 259 eV and a  $6 \times 6 \times 1$   $k$ -point mesh for the  $\sqrt{13} \times \sqrt{13}$  unit cell are used. All atoms were relaxed until the residual force components became smaller than 0.02 eV/Å. On-site Coulomb energy ( $U = 2.3$  eV) was included for Ta  $5d$  orbitals to reproduce the Mott gap size in experiment<sup>32</sup>. Similar calculation methods were successfully used in our previous study<sup>29</sup>.

## DATA AVAILABILITY

The authors declare that the data supporting the findings of this study are available within the article and its Supplementary Information.

Received: 1 December 2020; Accepted: 23 February 2021;

Published online: 22 March 2021

## REFERENCES

- Woods, C. R. et al. Commensurate-incommensurate transition in graphene on hexagonal boron nitride. *Nat. Phys.* **10**, 451 (2014).
- Cao, Y. et al. Unconventional superconductivity in magic-angle graphene superlattices. *Nature* **556**, 43 (2018).
- Naik, M. H. & Jain, M. Ultraflatbands and shear solitons in Moiré patterns of twisted bilayer transition metal dichalcogenides. *Phys. Rev. Lett.* **121**, 266401 (2018).
- Fazekas, P. & Tosatti, E. Charge carrier localization in pure and doped 1T-TaS<sub>2</sub>. *Phys. B+C* **99**, 183 (1980).
- May, M. M., Brabetz, C., Janowitz, C. & Mancke, P. Charge-density-wave phase of 1T-TiSe<sub>2</sub>: The influence of conduction band population. *Phys. Rev. Lett.* **107**, 176405 (2011).
- Yan, S. Y. et al. Influence of domain walls in the incommensurate charge density wave state of Cu intercalated 1T-TiSe<sub>2</sub>. *Phys. Rev. Lett.* **118**, 106405 (2017).
- Joe, Y. I. et al. Emergence of charge density wave domain walls above the superconducting dome in 1T-TiSe<sub>2</sub>. *Nat. Phys.* **10**, 2935 (2014).
- Xu, P. et al. Superconducting phase in the layered dichalcogenide 1T-TaS<sub>2</sub> upon inhibition of the metal-insulator transition. *Phys. Rev. B* **81**, 172503 (2010).
- Ang, R. et al. Superconductivity and bandwidth-controlled Mott metal-insulator transition in 1T-TaS<sub>2-x</sub>Se<sub>x</sub>. *Phys. Rev. B* **88**, 115145 (2013).
- Stojchevska, L. et al. Ultrafast switching to a stable hidden quantum state in an electronic crystal. *Science* **344**, 177 (2014).
- Vaskivskyi, I. et al. Controlling the metal-to-insulator relaxation of the metastable hidden quantum state in 1T-TaS<sub>2</sub>. *Sci. Adv.* **1**, e1500168 (2015).
- Vaskivskyi, I. et al. Fast electronic resistance switching involving hidden charge density wave states. *Nat. Commun.* **7**, 11442 (2016).
- Han, T.-R. T. et al. Exploration of metastability and hidden phases in correlated electron crystals visualized by femtosecond optical doping and electron crystallography. *Sci. Adv.* **1**, e1400173 (2015).
- Yoshida, M., Suzuki, R., Zhang, Y., Nkano, M. & Iwasa, Y. Memristive phase switching in two-dimensional 1T-TaS<sub>2</sub> crystals. *Sci. Adv.* **1**, e1500606 (2015).
- Tsen, A. W. et al. Structure and control of charge density waves in two-dimensional 1T-TaS<sub>2</sub>. *Proc. Natl Acad. Sci. USA* **112**, 15054 (2015).
- Zong, A. et al. Ultrafast manipulation of mirror domain walls in a charge density wave. *Sci. Adv.* **4**, eaau5501 (2018).
- Wen, W., Dang, C. & Xie, L. Photoinduced phase transitions in two-dimensional charge-density-wave 1T-TaS<sub>2</sub>. *Chin. Phys. B* **28**, 058054 (2019).
- Cho, D. et al. Nanoscale manipulation of the Mott insulating state coupled to charge order in 1T-TaS<sub>2</sub>. *Nat. Commun.* **7**, 10453 (2016).
- Ma, L. et al. A metallic mosaic phase and the origin of Mott insulating state in 1T-TaS<sub>2</sub>. *Nat. Commun.* **7**, 10956 (2016).
- Bu, K. et al. Possible strain induced Mott gap collapse in 1T-TaS<sub>2</sub>. *Comms. Phys.* **2**, 146 (2019).

21. Sakabe, D., Liu, Z., Suenaga, K., Nakatsugawa, K. & Tanda, S. Direct observation of mono-layer, bi-layer, and tri-layer charge density waves in 1T-TaS<sub>2</sub> by transmission electron microscopy without a substrate. *npj Quant. Mater.* **2**, 22 (2017).
22. Laulhé, C. et al. Ultrafast formation of a charge density wave state in 1T-TaS<sub>2</sub>: Observation at nanometer scales using time-resolved X-ray diffraction. *Phys. Rev. Lett.* **118**, 247401 (2017).
23. Avigo, I. et al. Excitation and relaxation dynamics of the photo-perturbed correlated electron system 1T-TaS<sub>2</sub>. *Appl. Sci.* **9**, 44 (2019).
24. Ang, R. et al. Real-space coexistence of the melted Mott state and superconductivity in Fe-substituted 1T-TaS<sub>2</sub>. *Phys. Rev. Lett.* **109**, 176403 (2012).
25. Liu, Y. et al. Nature of charge density waves and superconductivity in 1T-TaSe<sub>2-x</sub>Te<sub>x</sub>. *Phys. Rev. B* **94**, 045131 (2016).
26. Sipos, B. et al. From Mott state to superconductivity in 1T-TaS<sub>2</sub>. *Nat. Mater.* **7**, 960 (2008).
27. Li, L. J. et al. Controlling many-body states by the electric-field effect in a two-dimensional material. *Nature* **529**, 185 (2016).
28. Chen, C., Su, L., Castro Neto, A. H. & Pereira, V. M. Discommensuration-enhanced superconductivity in the charge density wave phases of transition-metal dichalcogenides. *Phys. Rev. B* **99**, 121108(R) (2019).
29. Park, J. W., Cho, G. Y., Lee, J. & Yeom, H. W. Emergent honeycomb network of topological excitations correlated charge density wave. *Nat. Commun.* **10**, 4038 (2019).
30. Pillo, T. et al. Interplay between electron-electron interaction and electron-phonon coupling near the Fermi surface of 1T-TaS<sub>2</sub>. *Phys. Rev. B* **62**, 4277 (2000).
31. Clerc, F. et al. Lattice-distortion-enhanced electron-phonon coupling and Fermi surface nesting in 1T-TaS<sub>2</sub>. *Phys. Rev. B* **74**, 155114 (2006).
32. Cho, D., Cho, Y.-H., Cheong, S.-W., Kim, K.-S. & Yeom, H. W. Interplay of electron-electron and electron-phonon interactions in the low-temperature phase of 1T-TaS<sub>2</sub>. *Phys. Rev. B* **92**, 085132 (2015).
33. Lawa, K. T. & Lee, P. A. 1T-TaS<sub>2</sub> as a quantum spin liquid. *Proc. Natl Acad. Sci. USA* **114**, 6996 (2017).
34. Klanjšek, M. et al. A high-temperature quantum spin liquid with polaron spins. *Nat. Phys.* **13**, 1130 (2017).
35. Brouwer, R. & Jellinek, F. The low-temperature superstructures of 1T-TaSe<sub>2</sub> and 2H-TaSe<sub>2</sub>. *Phys. B+C* **99**, 51 (1980).
36. Cho, D. et al. Correlated electronic states at domain walls of a Mott-charge-density-wave insulator 1T-TaS<sub>2</sub>. *Nat. Commun.* **8**, 392 (2017).
37. Wu, X. L. & Lieber, C. M. Hexagonal domain-like charge density wave phase of TaS<sub>2</sub> determined by scanning tunneling microscopy. *Science* **243**, 1704 (1989).
38. Nakanishi, K., Takatera, H., Yamada, Y. & Shiba, H. The nearly commensurate phase and effect of harmonics on the successive phase transition in 1T-TaS<sub>2</sub>. *J. Phys. Soc. Jpn.* **43**, 1509 (1977).
39. Yamamoto, A. Hexagonal domainlike structure in 1T-TaS<sub>2</sub>. *Phys. Rev. B* **27**, 7823 (1983).
40. Wu, X. L. & Lieber, C. M. Direct observation of growth and melting of the hexagonal-domain charge-density-wave phase in 1T-TaS<sub>2</sub> by scanning tunneling microscopy. *Phys. Rev. Lett.* **64**, 1150 (1990).
41. Burk, B., Thomson, R. E., Zettl, A. & Clarke, J. Charge-density-wave domains in 1T-TaS<sub>2</sub> observed by satellite structure in scanning-tunneling-microscopy images. *Phys. Rev. Lett.* **66**, 3040 (1991).
42. Spijkerman, A., de Boer, J. L., Meetsma, A. & Wieggers, G. A. X-ray crystal-structure refinement of the nearly commensurate phase of 1T-TaS<sub>2</sub> in (3+2)-dimensional superspace. *Phys. Rev. B* **56**, 1357 (1997).
43. Lee, J. M. et al. Stable flatbands, topology, and superconductivity of magic honeycomb networks. *Phys. Rev. Lett.* **124**, 137002 (2020).
44. Kratochvilova, M. et al. The low-temperature highly correlated quantum phase in the charge-density-wave 1T-TaS<sub>2</sub> compound. *npj Quant. Mater.* **2**, 42 (2017).
45. Pal, S. et al. Possible glass-like random singlet magnetic state in 1T-TaS<sub>2</sub>. *J. Phys.* **32**, 035601 (2020).
46. Su, W. P., Schrieffer, J. R. & Heeger, A. K. Solitons in polyacetylene. *Phys. Rev. Lett.* **42**, 1698 (1979).
47. Skolimowski, J., Gerasimenko, Y. & Žitko, R. Mottness collapse without metallization in the domain wall of the triangular-lattice Mott insulator 1T-TaS<sub>2</sub>. *Phys. Rev. Lett.* **122**, 036802 (2019).
48. Gerasimenko, Y. A., Karpov, P., Vaskivskiy, I., Brazovskii, S. & Mihailovic, D. Intertwined chiral charge orders and topological stabilization of the light-induced state of a prototypical transition metal dichalcogenide. *npj Quant. Mater.* **4**, 32 (2019).
49. Kresse, G. & Furthmüller, J. Efficient iterative schemes for *ab initio* total-energy calculations using a plane-wave basis set. *Phys. Rev. B* **54**, 11169 (1996).
50. Perdew, J. P., Burke, K. & Ernzerhof, M. Generalized gradient approximation made simple. *Phys. Rev. Lett.* **77**, 3865 (1996).
51. Blöchl, P. E. Projector augmented-wave method. *Phys. Rev. B* **50**, 17953 (1994).

## ACKNOWLEDGEMENTS

This work was supported by Institute for Basic Science (Grant No. IBS-R014-D1).

## AUTHOR CONTRIBUTIONS

H.W.Y. supervised the research. J.W.P. performed the DFT calculations. J.L. carried out the STM experiment. J.W.P. and H.W.Y. analyzed the data and wrote the manuscript with the comments of all other authors.

## COMPETING INTERESTS

The authors declare no competing interests.

## ADDITIONAL INFORMATION

**Supplementary information** The online version contains supplementary material available at <https://doi.org/10.1038/s41535-021-00330-9>.

**Correspondence** and requests for materials should be addressed to J.W.P. or H.W.Y.

**Reprints and permission information** is available at <http://www.nature.com/reprints>

**Publisher's note** Springer Nature remains neutral with regard to jurisdictional claims in published maps and institutional affiliations.



**Open Access** This article is licensed under a Creative Commons Attribution 4.0 International License, which permits use, sharing, adaptation, distribution and reproduction in any medium or format, as long as you give appropriate credit to the original author(s) and the source, provide a link to the Creative Commons license, and indicate if changes were made. The images or other third party material in this article are included in the article's Creative Commons license, unless indicated otherwise in a credit line to the material. If material is not included in the article's Creative Commons license and your intended use is not permitted by statutory regulation or exceeds the permitted use, you will need to obtain permission directly from the copyright holder. To view a copy of this license, visit <http://creativecommons.org/licenses/by/4.0/>.

© The Author(s) 2021